TeO_2 glass properties from first principles

F. Pietrucci,* S. Caravati,† and M. Bernasconi
Dipartimento di Scienza dei Materiali, Università di Milano-Bicocca, Via R. Cozzi 53, I-20125 Milano, Italy
(Received 30 October 2007; revised manuscript received 8 July 2008; published 8 August 2008)

Based on *ab initio* molecular-dynamics simulations, we have investigated the properties of TeO_2 glass generated by fast quenching from the liquid phase. Structural properties of the glass model are in good agreement with available diffraction data. Inspection on the local structure of the glass phase reveals the presence of a great variety of Q_m^n polyhedra with the predominance of Q_4^4 units typical of the crystalline phases of TeO_2. Calculated IR and Raman spectra of amorphous TeO_2 are in good agreement with experimental data and provide an assignment of the most prominent experimental peaks to specific phonons.

DOI: 10.1103/PhysRevB.78.064203 PACS number(s): 78.30.−j, 71.55.Jv, 63.50.−x

I. INTRODUCTION

Tellurite glasses are considered good candidate materials for optical switching devices due to their large nonlinear susceptibility, the largest among known glasses.[1] TeO_2 glasses have also been proposed as active material in optical amplifiers due to their large cross section for stimulated Raman scattering (SRS). These functional properties are strongly affected by the insertion of modifiers such as alkali oxides (e.g., Na_2O and Li_2O) or transition-metal oxides (e.g., V_2O_3 and WO_3) which are added to enhance the ease of glass formation and the stability against crystallization. In particular, tellurite glasses stabilized by heavy transition-metal oxides such as WO_3 and Nb_2O_5 have been recently reported to display a Raman-scattering cross-section of 2 orders of magnitude larger than that of silica glasses, already used as SRS amplifiers, and 1 order of magnitude larger than that of alkali-doped tellurite glasses.[2,3] Pure TeO_2 glass has also been synthesized in the form of thin film by sol-gel processing[4,5] and by fast quenching from the melt.[6] In spite of its potential technological importance, the microscopic description of the structure of TeO_2 glass and of the bonding network modifications induced by the stabilizers is largely incomplete.

In this work, we provide insight into the properties of TeO_2 glass (g-TeO_2) investigating a model of the glass generated by quenching from the melt within *ab initio* molecular-dynamics (MD) simulations based on density-functional theory (DFT). We have validated this framework on tellurite crystals by computing the structural and vibrational properties of the crystalline phases (α, β, and γ) of pure TeO_2 and of Li_2TeO_3 in previous works.[7,8]

The paper is organized as follows. We briefly review previous experimental works on the structure of g-TeO_2 in Sec. II. In Sec. III we outline the computational details; in Sec. IV we report the results of the simulations on liquid TeO_2 (at 2400 and 1000 K) which has been used to generate the glass model upon quenching. The structural, electronic, and vibrational properties of our g-TeO_2 model are presented in Sec. V, and finally Sec. VI is devoted to our conclusions.

II. REVIEW OF PREVIOUS WORKS ON THE STRUCTURE OF g-TeO_2

The traditional view of the structure of glassy TeO_2 as a distorted lattice of the crystalline paratellurite phase α-TeO_2 has been challenged recently by the discovery of another crystalline phase of TeO_2, γ-TeO_2.[9,10] By heating the glass, the metastable γ phase crystallizes first. Only upon further thermal annealing the α phase is obtained. This fact would suggest that the γ phase is somehow closer to the structure of the glass with respect to the α phase.[10] Magic angle spinning (MAS)-NMR studies of ^{125}Te identified several structural units in tellurite glasses;[11,12] different NMR peaks have been assigned to TeO_m units where Te is either tetracoordinated ($m=4$) or threefold coordinated ($m=3$). In turn, the O atoms of the TeO_m units can be bridging (BO) (connecting two Te ions) or nonbridging (NBO). These structures have been referred to by introducing the notation Q_m^n, where m is the number of bonded O ions (within a cutoff $R_{max}=2.36$ Å chosen to include the bond-length distribution of TeO_2-based crystals[13]) and n is the number of bonded O ions which are also bridging to other Te ions. According to this notation, illustrated in Fig. 1, the crystalline α-, β-, and γ-TeO_2 phases consist of Q_4^4 units (i.e., fully connected corner-sharing trigonal bipyramids) whereas metal-tellurite crystals comprise the four units Q_4^3, Q_3^2, Q_3^1, and Q_3^0. The Q_4^4 unit has the shape of a trigonal bipyramid with two shorter Te-O_{eq} equatorial bonds (1.86–1.95 Å), two longer Te-O_{ax} axial bonds (2.02–2.20 Å), and a lone electron pair on Te in the equatorial plane (Fig. 1). In paratellurite (α-TeO_2), the Q_4^4 units form a three-dimensional (3D) fully connected structure,[14] while β-TeO_2 has a layered structure with weakly bonded sheets.[15] In γ-TeO_2, one Te-O bond is substantially longer than the other three and, by breaking this latter bond, a

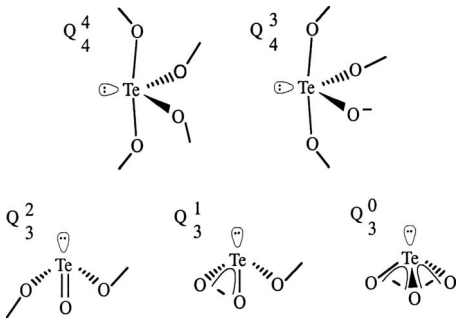

FIG. 1. Coordination polyhedra Q_m^n of Te atom found in tellurite crystals, with m=number of bonded O atoms and n=number of bridging O atoms. Adapted from Ref. 13.

chainlike structure appears. The γ-TeO_2 phase has then been described also in terms of a polymeric form made of TeO_3 units (Q_3^2 polyhedra if R_{max} is reduced below 2.2 Å).[9,10] However, we also mention that lattice dynamics calculations revealed that the phononic spectra of α-TeO_2 and β-TeO_2 can be well interpreted in terms of vibrations of weakly coupled TeO_2 molecules.[10,16–18] Accordingly, tellurite and paratellurite would be seen as molecular crystals made of TeO_2 molecules. The polymeric γ-TeO_2 would represent a chainlike polymerization of TeO_2 molecules giving rise to a structure more connected than paratellurite and tellurite phases. However, the calculated elastic constants and electronic band structure do not show strong anisotropies which would have been expected from the description of γ-TeO_2 as the assembling of aligned polymers.[7] As a matter of fact, TeO_2 molecules in α- and β-TeO_2 and polymerized TeO_2 chains in γ-TeO_2 are strongly interacting, possibly via electrostatic coupling, as suggested by the strong ionic character of the Te-O bond emerged from previous *ab initio* calculations.[19,20]

Models of alkali-stabilized tellurite glasses have been generated by a reverse Monte Carlo (RMC) fitting of neutron and x-ray diffraction data.[13,21] These models contain a large number of NBO ions. It has then been proposed that the stabilization against recrystallization induced by the alkali dopant might be due to the presence of many different Q_m^n units whose conversion into the Q_4^4 unit of TeO_2 crystals would require a large reorganization of the network.[13]

Although these latter works represent a big step toward the understanding of the microscopic structure of tellurite glasses, both the NMR analysis based on comparisons with crystalline analogs and the reverse Monte Carlo models fitted on experimental total pair-correlation functions are subject to large uncertainties. In alkali-doped tellurite glasses, for instance, the total pair-correlation function is actually the sum of six partial pair-correlation functions. A compelling identification of the proposed structural units, of their interaction in the network and evolution with the addition of modifiers are still matter of debate. In this respect, *ab initio* simulations can be of great help in providing a reliable model of the glass structure as demonstrated, for instance, by Car-Parrinello (CP) molecular-dynamics simulations of a-SiO_2.[22,23]

III. COMPUTATIONAL DETAILS

Liquid and glassy TeO_2 have been modeled by a cubic supercell of side 11.3 Å containing 32 TeO_2 f.u., which corresponds to the experimental density of the glass at normal conditions [ρ_{expt}=5.84 g/cm^3 (Ref. 24)]. Periodic boundary conditions have been applied. *Ab initio* molecular-dynamics simulations have been performed in the framework of density-functional theory with gradient corrected exchange and correlation functional [Becke-Lee-Yang-Parr (BLYP)].[25,26] The BLYP functional has been chosen since it performed marginally better than others [Perdew-Burke-Ernzerhof (PBE)] in reproducing the vibrational spectra of the crystalline phases of TeO_2.[7] Born-Oppenheimer molecular-dynamics simulations have been performed in the Quickstep scheme,[27,28] as implemented in the code CP2K.[29] In this approach Kohn-Sham orbitals are expanded on a Gaussian basis set, whereas an auxiliary plane-wave expansion of the electronic density is used to efficiently evaluate the Hartree part of the Coulomb interactions and the exchange-correlation energy. Goedecker-type pseudopotentials[30] and double-zeta plus polarization (DZVP) Gaussian basis sets for O and Te have been used. A kinetic cutoff of 240 Ry has been used for the plane-wave expansion of the density. Basis sets and cutoffs have been tested on the isolated TeH_2 and TeO_2 molecules, obtaining in both cases 1% error on the bond lengths and 0.1% error on the bond angles compared to experiments. The equations of motion are integrated with the velocity Verlet algorithm with a time step δt=1.5 fs. As it will be discussed in Sec. IV, we have generated two glassy models according to two quenching protocols, a short one and a much longer one, in order to assess the dependence of the glass structure on the quenching time. For the second protocol lasting 80 ps, we have used a recent approach to *ab initio* molecular dynamics presented by Kuhne *et al.*[31] which allows speeding up the simulations by 1 order of magnitude for the system size we have used. In the spirit of the CP approach, the wave function is not self-consistently optimized during the dynamics. However, in contrast to CP, large integration time steps can be used in the simulation. This scheme leads to a slightly dissipative dynamics of the type $-\gamma_D \dot{\mathbf{R}}_I$, where $\mathbf{R}_I$ are the ionic coordinates. In Ref. 31 it is shown how to compensate for this dissipation and obtain a correct canonical sampling. The electronic problem is solved as detailed above for standard Born-Oppenheimer molecular dynamics. Simulations of the liquid phase have also been repeated with a larger basis set triple-zeta plus polarization (TZVP) with negligible change in structural and dynamical properties. The electronic, vibrational, and Raman properties of the glass model have been investigated by making use of a plane-wave expansion of Kohn-Sham orbitals up to a kinetic cutoff of 70 Ry and norm-conserving pseudopotentials,[32] as implemented in the CPMD code.[33] Brillouin-zone sampling has been restricted to the Γ point only of a 96-atom cubic supercell. The vibrational spectrum of the glass model is obtained by calculating the dynamical matrix from finite atomic displacements. Effective charges and the electronic dielectric tensor are calculated by density-functional linear perturbation theory[34] as implemented in the CPMD code.[33] Details on the calculation of the vibrational spectra, Raman, and IR response are given in Sec. IV. Car-Parrinello[35] molecular-dynamics simulations at room temperature and 1000 K have also been performed as a further test of the completeness of the Gaussian-type basis set. We have used a time step δt=7 a.u. (0.17 fs) and a fictitious electronic mass μ=1000 a.u.

IV. LIQUID TeO_2

We have equilibrated at high temperature a model of liquid TeO_2 later used for the generation of the glass model upon quenching. Starting from an initial configuration formed by randomly placed TeO_2 molecules, we performed a microcanonical (*NVE*) Born-Oppenheimer molecular-dynamics simulation of 3 ps long at an average temperature

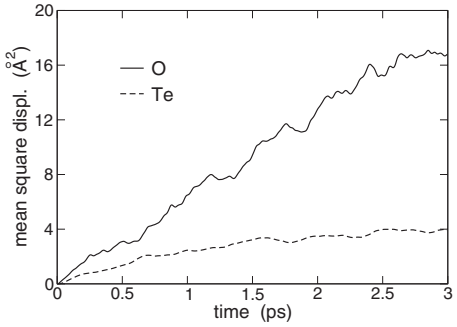

FIG. 2. Mean-square displacement of atoms in liquid tellurite at $T=2400$ K.

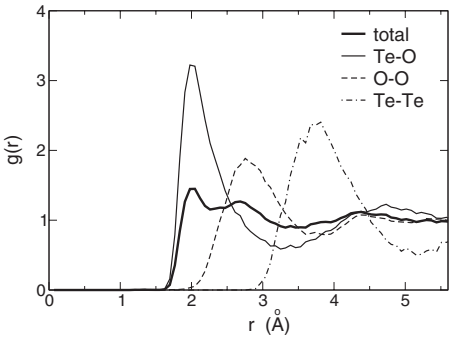

FIG. 3. Pair distribution functions (partial and total) of the liquid tellurite model averaged over 1 ps of molecular-dynamics simulation at $T=2400$ K (extending the time average over 2 ps the results do not change appreciably on the scale of the figure). The density corresponds to the experimental density of the glass (see text).

of 2400 K, well above the experimental glass-transition temperature [$T_g \approx 580$ K (Ref. 24)]. The system has then been quenched in 8 ps and equilibrated at 1000 K. Since the simulations of the liquid are instrumental to the generation of the glass and experimental data on the density of the high-temperature liquid are lacking, we have not attempted to optimize the density of the liquid at different temperatures. Instead, we have fixed the density to the experimental density of the glass [$\rho_{\text{expt}}=5.84$ g/cm^3 (Ref. 24)]. As a result, our liquid models are pressurized, the calculated pressure at 2500 and 1000 K being of the order of 15 and 8 GPa, respectively. Although the properties of our liquid models cannot be compared directly with experimental data at normal pressure (which are lacking as well), we think they deserve an analysis also for sake of comparison with the properties of the glass. Results at high (2400 K) and at low (1000 K) temperatures are reported separately in Secs. IV A and IV B.

A. High-temperature liquid

At 2400 K, Te and O atoms diffuse on average by 2.0 and 4.1 Å (in 3 ps), respectively (Fig. 2), sufficiently far to explore several local configurations since Te–O bond lengths in the crystalline phases are in the range 1.9–2.2 Å.[7] The self-diffusion coefficients D estimated from the mean-square displacement ($D=\lim_{t\to\infty}\langle|\mathbf{R}(t)-\mathbf{R}(0)|^2\rangle/6t$) in the last 2 ps of the simulation are $D_{\text{Te}} \approx 1.3\times10^{-5}$ cm^2/s and $D_{\text{O}} \approx 1.0\times10^{-4}$ cm^2/s.

The theoretical partial pair-correlation functions $g_{\alpha\beta}(r)$ of Te–O, O–O, and Te–Te pairs are reported in Fig. 3. The function $g_{\alpha\beta}(r)$ gives the ratio between the density of atoms of species β at a distance r from an atom of species α and the average density ρ_β of atoms of species β as[36]

$$g_{\alpha,\beta}(r) = \frac{1}{N_\alpha \rho_\beta} \sum_{I\in\alpha, J\in\beta} \langle \delta(\mathbf{r}+\mathbf{R}_I-\mathbf{R}_J)\rangle, \quad (1)$$

where N_α is the number of atoms of species α. The total pair-correlation function is given in turn by[36]

$$g(r) = \sum_{\alpha\beta} x_\alpha x_\beta g_{\alpha\beta}(r), \quad (2)$$

where x_α is the number concentration of species α.

The main peaks of the partial pair-correlation functions are centered around 2.0, 2.8, and 3.7 Å for Te–O, O–O, and Te–Te pairs, respectively, which are within the range of the typical interatomic distances in the three crystalline phases of TeO_2.[7] The Te–O pair-correlation function is rather broad with the first minimum above 3.3 Å. At such a long interatomic separation Te and O can hardly be considered to form a bond. To analyze the structure of the liquid and for sake of comparison with the glass that will be discussed later on, we have used for the definition of the bond the cutoff distance $R_{\max}=2.36$ Å which corresponds to the position of first minimum of the $g_{\text{TeO}}(r)$ pair-correlation function in the glass (Fig. 12). The coordination numbers of Te and O atoms are 3.42 and 1.95, respectively. The time-averaged distribution of coordination numbers is shown in the inset of Fig. 4. Most oxygen atoms are onefold or twofold coordinated with a tiny fraction of threefold coordinated atoms. To our knowledge experimental diffraction data for the liquid phase, to compare our results with, have been reported only for alkali tellurite $(K_2O)_x$-$(TeO_2)_{1-x}$ ($x=0.1-0.25$) (Refs. 37 and 38) but not for pure TeO_2.

The O–Te–O bond angle distribution of liquid TeO_2 (Fig. 4) shows several structures: a main broad peak centered at 85° and a broad double peak in the range 140°–165° which spans the range of the O_{eq}–Te–O_{eq} and O_{ax}–Te–O_{ax} angles in the crystalline phases (99°, 102°, 103° and 154°, 166°, 168°,

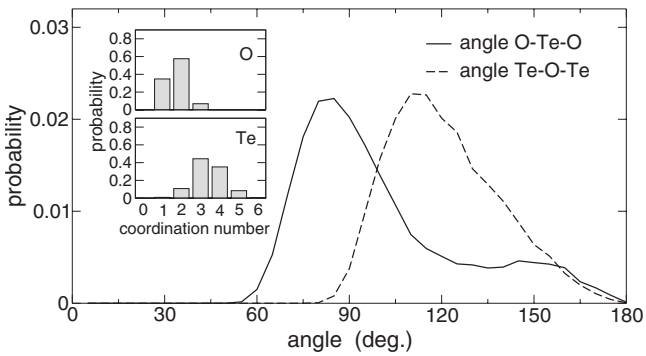

FIG. 4. O–Te–O and Te–O–Te angle distributions of liquid tellurite averaged over 1 ps of molecular-dynamics simulation at $T=2400$ K (extending the time average over 2 ps the results do not change appreciably on the scale of the figure). Inset: time-averaged distribution of coordination numbers.

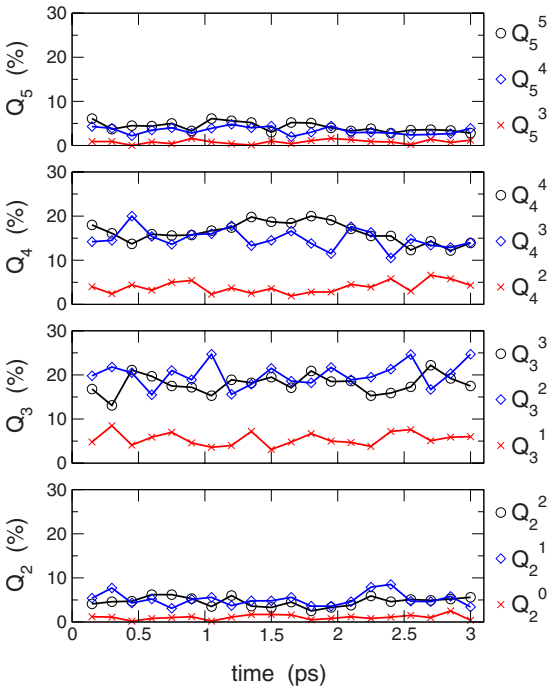

FIG. 5. (Color online) Evolution of the population of Q_m^n structural units as a function of time in liquid TeO_2 at $T=2400$ K. Only species in concentration larger than 1% are shown.

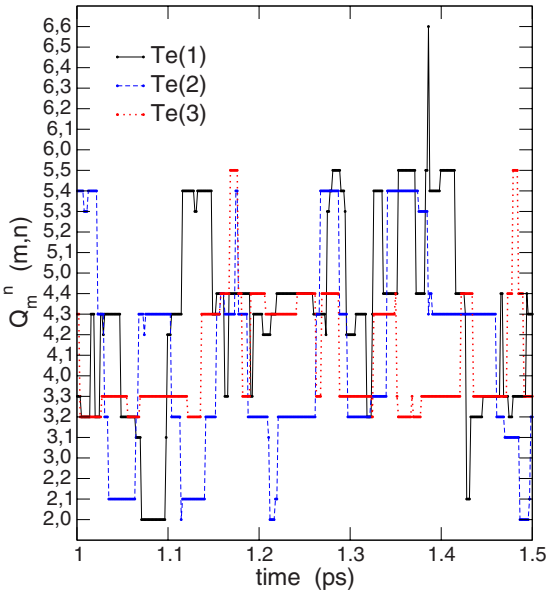

FIG. 6. (Color online) Time evolution of the type of Q_m^n polyhedra defining the environment of three selected Te atoms in liquid TeO_2 at 2400 K. The Q_m^n character is indicated by the couple of integers m,n. All other Te ions, not considered here, display a similar behavior.

respectively).[7] We also recall that the O–Te–O angle in the gas phase TeO_2 molecule is 112°.

The local environment around Te atoms is identified by the polyhedra Q_m^n described in Sec. I. For the definition of Te–O bond we employ the cutoff distance $R_{max}=2.36$ Å as discussed above. The same value of R_{max} has been used in the analysis of glass models generated by reverse Monte Carlo techniques[13] (see Sec. V for further discussion on the choice of R_{max}).

The distribution of Q_m^n polyhedra in our liquid model (Fig. 5) reveals the presence of several Q_m^n units, mainly Q_4^4, Q_4^3, Q_3^3, and Q_3^2. Each of them contributes more than 12% to the total polyhedra population, while lower-coordinated and lower-connected units Q_4^2, Q_3^1, Q_2^2, and Q_2^1 contribute less than 10% each. In particular, Q_2^0 units, corresponding to isolated TeO_2 molecules, are present in negligible concentration. Conversely, the concentration of the five-coordinated and highly connected Q_5^5 and Q_5^4 units is non-negligible (≈5% each). The Q_m^n populations undergo sizable oscillations during the 3 ps of simulation at high temperature (cf. Fig. 5) but always with a clear prominence of three- and four-coordinated Te atoms with at most one nonbridging O. The distribution of the Q_m^n structural units has a meaning only as a time average. In fact, at high temperature the atoms, especially O, diffuse very fast inducing a continuous variation of the coordination shell of each Te atom over the range of possible Q_m^n units. The average survival time of individual Q_m^n units is of the order of $\tau\sim 13$ fs (see Fig. 6). We have not observed a sizable dependence of the survival time on the type of Q_m^n polyhedra. The average concentration of Q_m^n units is reported in Table I. We have also found that TeO_2 molecular units defined by O_{eq}–Te–O_{eq} have a similar lifetime of 20 fs. The equatorial O atoms are identified once the axial atoms are found. The latter can be easily identified since O_{ax}–Te–O_{ax} angles are much larger than O_{eq}–Te–O_{eq} and O_{ax}–Te–O_{eq} angles.

B. Low-temperature liquid

In order to calculate the properties of liquid TeO_2 at a temperature accessible to experiments, we have equilibrated the liquid at $T\sim 1000$ K. Equilibration has been achieved in two independent simulations, a Quickstep simulation 30 ps long and a Car-Parrinello simulation[35] 10 ps long. Hereafter, we report the results of the CP simulation. Compared to the simulation at $T=2400$ K (Sec. IV A), the mean-square displacement of Te and O ions is strongly reduced (Fig. 7) but still shows a diffusive liquidlike behavior.

The Te–O, O–O, and Te–Te main peaks of the partial pair-correlation functions (Fig. 8) are centered around 1.93, 2.78, and 3.70 Å, respectively. A most-probable Te–O distance of 1.93 Å has also been observed in neutron-scattering experiments on liquid tellurite at $T=850$ K,[38] although including a stabilizer (K_2O, 20 mol %). For the definition of Te–O bond we employ the cutoff distance $R_{max}=2.36$ Å as for the high-temperature liquid.

TABLE I. Distribution (%) of Q_m^n structural units in liquid TeO_2 at $T=2400$ K and at $T=1000$ K, averaged over 3 and 10 ps, respectively.

	Q_3^1	Q_3^2	Q_3^3	Q_4^2	Q_4^3	Q_4^4	Q_5^4	Q_5^5
2400 K	5.2	19.1	18.6	3.7	14.1	17.5	3.2	6.5
1000 K	2.6	17.7	21.7	1.2	14.4	31.7	1.8	7.9

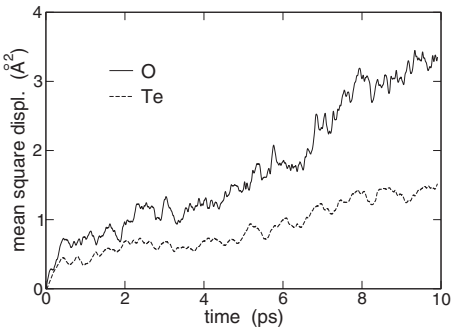

FIG. 7. Mean-square displacement of atoms in liquid tellurite at $T=1000$ K.

The average coordination numbers of Te and O atoms are 3.67 and 1.89, respectively. The time-averaged distribution of coordination numbers is shown in the inset of Fig. 9. The O–Te–O angular distribution shows two well-defined peaks centered around 90° and 160° (Fig. 9).

The populations of Q_m^n structural units oscillate in time during the simulation, as shown in Fig. 10, around the average values reported in Table I. Compared to the populations at $T=2400$ K, the Q_2^n units have disappeared whereas the fully connected Q_3^3, Q_4^4, and Q_5^5 units have increased at the expense of the less connected ones. At 1000 K, TeO_2 molecular units survive on average as long as 140 fs, while the survival time of individual Q_m^n units is 150 fs.

V. TeO_2 GLASS

A. Structural properties

The liquid has been quenched to room temperature by rescaling the atomic velocities in a Quickstep molecular-dynamics simulation according to two protocols, a shorter one and a longer one, hereafter referred to as protocols A and B, respectively. For the longer protocol B, the wave-function propagation is performed in the scheme of Ref. 31 (cf. Sec. III). The change in temperature as a function of time in the two quenching protocols is shown in Fig. 11. The short quenching time in protocol A amounts to a very high cooling rate of $\approx 10^{14}$ K/s. Fully relaxed model of TeO_2 glass has

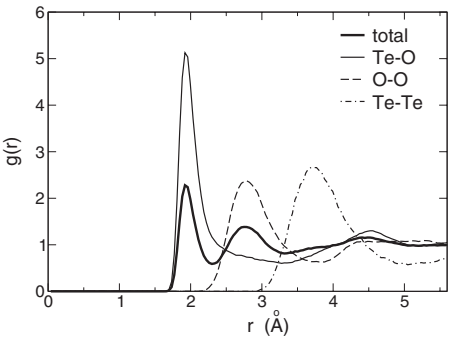

FIG. 8. Pair distribution functions (partial and total) of the liquid tellurite model averaged over 10 ps of molecular-dynamics simulation at $T=1000$ K. The density corresponds to the experimental density of the glass (see text).

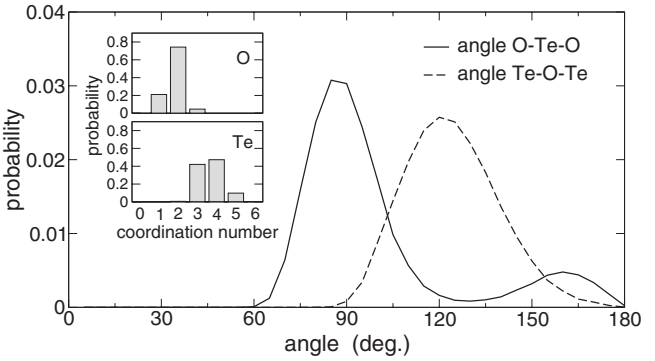

FIG. 9. O–Te–O and Te–O–Te angle distributions of liquid tellurite averaged over 10 ps of molecular-dynamics simulation at $T=1000$ K. Inset: time-averaged distribution of coordination numbers.

been obtained by geometry optimization from the room-temperature simulations. Structural, electronic, and vibrational properties of the optimized model have been computed with the code CPMD (cf. Sec. III).

To compare our results with experimental structural data recorded at room temperature we have further equilibrated the as-quenched model in a 3 ps microcanonical (*NVE*) molecular-dynamics simulation at an average temperature of 300 K. The structural properties of the two glassy models generated by protocols A and B are very similar with tiny and nearly indistinguishable differences on the scale of the figures that will be reported below. Therefore, hereafter we will discuss the properties of model A if not otherwise specified.

The pair-correlation functions and the O–Te–O bond angle distribution of g-TeO_2 are shown in Figs. 12 and 13, respectively. The $g_{TeO}(r)$ partial correlation function has a sharp peak in the range 1.9–2.2 Å (with a tail up to 2.4 Å), which means that Te–O bond lengths in the glass span the same range as in the crystalline phases. The average coordination numbers computed by integrating the partial pair-

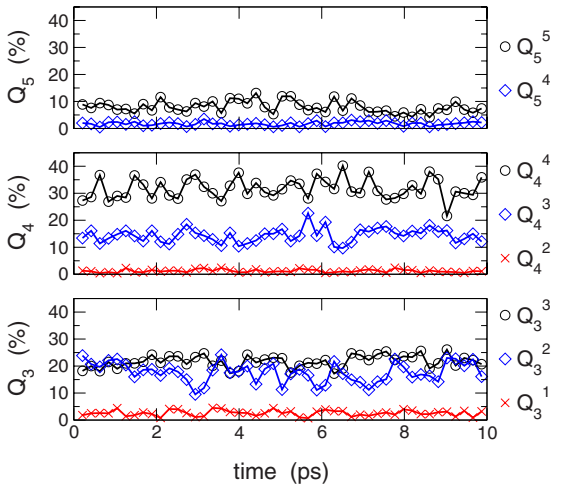

FIG. 10. (Color online) Evolution of the population of Q_m^n structural units as a function of time in liquid TeO_2 at $T=1000$ K. Only species in concentration larger than 1% are shown.

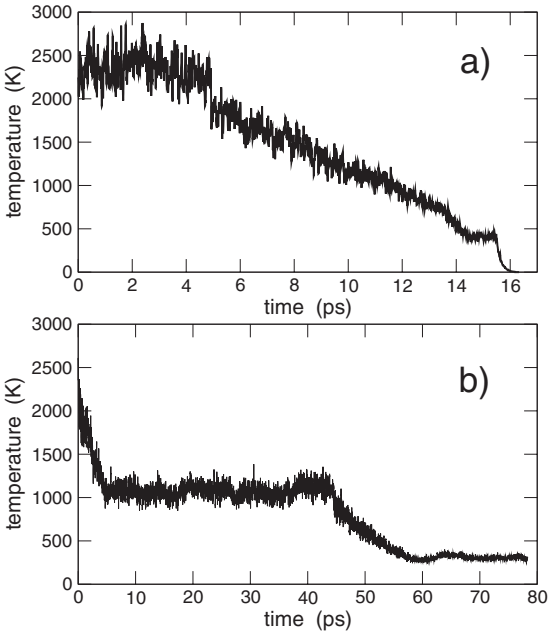

FIG. 11. Temperature of the TeO_2 model as a function of time. (a) Quenching from the melt within Born-Oppenheimer molecular dynamics. (b) Quenching from the melt within the *ab initio* molecular-dynamics scheme of Kühne *et al.* (Ref. 31) (see text).

correlation functions up to the first minimum (2.36 Å) are 3.69 and 1.85 for Te and O, respectively. The time-averaged distribution of coordination numbers is shown in the inset of Fig. 13.

Since the neutron-scattering lengths of Te and O are equal (b_O=5.80 and b_{Te}=5.803) (Ref. 39) the total $g(r)$ given in Eq. (2) can be compared directly with the experimental total pair correlation obtained by Fourier transforming the total neutron structure factor.[36] The experimental[6] and theoretical total $g(r)$ compared in Fig. 12 are in good agreement, with a slightly broader distribution of Te–O bond lengths in the real glass compared to our model. Experimental data are taken on pure TeO_2 glass produced by fast quenching from the melt. The first peak of $g_{TeO}(r)$ shows a shoulder around 2.1 Å

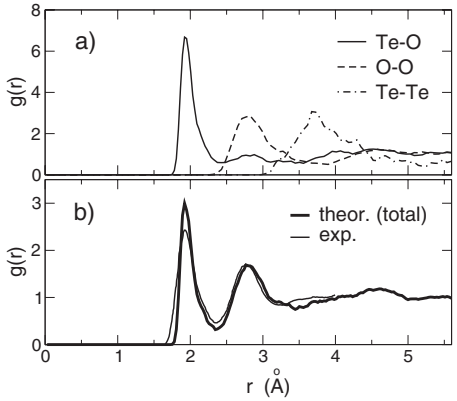

FIG. 12. (a) Partial pair-correlation functions $g_{\alpha\beta}(r)$ of the tellurite glass model at 300 K averaged over 2 ps. (b) Total pair-correlation function $g(r)$ compared with experimental neutron-diffraction data adapted from Ref. 6 (see text).

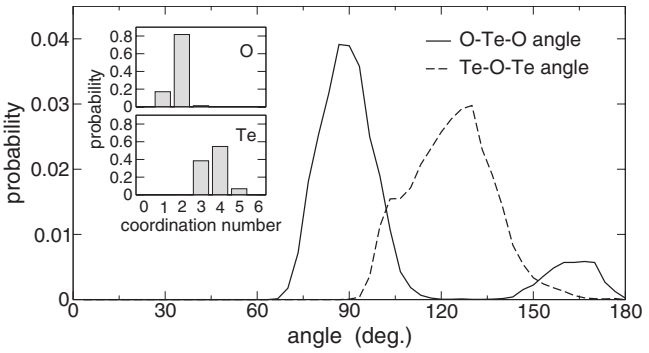

FIG. 13. O–Te–O and Te–O–Te angle distribution functions in the model of g-TeO_2 at room temperature.

which could be interpreted as due to the longer equatorial Te–O bonds. Indeed, experimentally the function $J(r)=4\pi r^2\bar{\rho}g(r)$ ($\bar{\rho}$=number density) has been decomposed in the sum of two Gaussian functions centered at about 1.90 and 2.15 Å which should represent short equatorial-like and long axial-like Te–O bonds, respectively.[7] The similarity between the models produced by the two protocols indicates that the average structural properties do not depend sizably on the quenching time on the time scale of 5–20 ps. We cannot obviously exclude that a quenching time of several orders of magnitude longer than here investigated might change the structure considerably. However, the good agreement between theoretical and experimental structural data gives us confidence on the reliability of our models.

The O–Te–O angle distribution shows two distinct peaks: the weaker spans the range 150°–170° as the O_{ax}–Te–O_{ax} angles in the crystalline phases and the stronger spans the range 70°–105° which includes the O_{eq}–Te–O_{eq} angles (99°–103°) and the O_{eq}–Te–O_{ax} angles of the α, β, and γ phases.[7] We here recall that the calculation of the bond angle distribution function is based on a criterion to assign a bond. As already stated, two atoms are assumed to be bonded when their distance is below a cutoff distance chosen, as usual, as the first minimum of the partial pair-correlation function R_{max}=2.36 Å (cf. Fig. 12) which also corresponds to the cutoff distance used in the analysis of glass models generated by reverse Monte Carlo techniques.[13] This geometrical definition of the bond is corroborated in our system by the presence of a Wannier function of the oxygen along the interatomic separation (cf. Sec. V B).

Partial $S_{\alpha\beta}(Q)$ and total $S(Q)$ structure factors have also been computed as a function of the exchange momentum Q. They are reported for future reference whenever neutron scattering on isotopically substituted samples would be available. The partial structure factor is given by

$$S_{\alpha\beta}(Q)=\frac{1}{\sqrt{N_\alpha N_\beta}}\left[\left\langle\sum_{I=1}^{N_\alpha}\sum_{J=1}^{N_\beta}e^{-i\mathbf{Q}\cdot(\mathbf{R}_I-\mathbf{R}_J)}\right\rangle-\delta_{\mathbf{Q},0}\right], \quad (3)$$

where, following Ref. 40, the thermal average $\langle\cdots\rangle$ is computed from harmonic phonons as

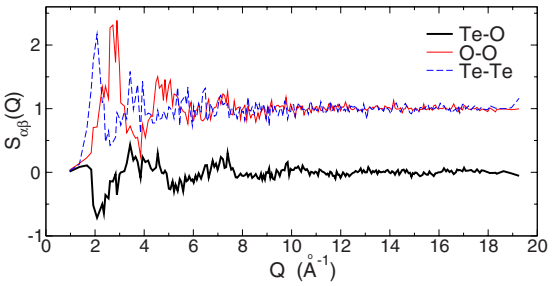

FIG. 14. (Color online) Theoretical partial structure factors of TeO_2 glass.

$$\langle \mathbf{R}_\kappa \mathbf{R}_{\kappa'} \rangle = \sum_j \frac{\hbar}{\omega_j} \frac{\mathbf{e}(j,\kappa)}{\sqrt{M_\kappa}} \frac{\mathbf{e}(j,\kappa')}{\sqrt{M_{\kappa'}}} \left[n_B(\omega_j) + \frac{1}{2} \right], \quad (4)$$

where M_κ is the mass of κth atom and ω_j and $\mathbf{e}(j,\kappa)$ are frequencies and eigenvector of the jth harmonic phonon (computed as will be discussed in Sec. V C). The temperature dependence is introduced by the Bose factor $n_B(\omega_j)$.

Since the neutron-scattering lengths of Te and O are equal, the neutron total structure factor can be obtained from the partial structure factors simply by[36]

$$S(Q) = \sum_{\alpha\beta} (x_\alpha x_\beta)^{1/2} S_{\alpha\beta}(Q). \quad (5)$$

The partial structure factors of our g-TeO_2 model are shown in Fig. 14 and the total structure factor is compared with the experimental data from neutron diffraction in Fig. 15.

Insight on the local structure of the glass can be obtained by inspection on the distribution of Q_m^n polyhedra reported in Table II. This has been obtained by averaging over the two models A and B. The time average over a single model introduces deviation of less than 3% with respect to the data in Table II. The threshold in the Te–O bond length used to assign the Q_m^n polyhedra is still R_{max}=2.36 Å. The main structural unit is Q_4^4, but more than half of the Te atoms show different local environment. This clearly indicates that TeO_2 glass is not simply a random network formed by the Q_4^4 structural units found in the crystalline phases. Actually, 14% of the O atoms are terminal atoms bonded to one Te atom only (NBO), while only 1% of O atoms are bonded to three Te atoms. Many three-coordinated Te atoms (38%) are present in the glass, as well, while coordinations lower than three are absent. Our glass model also shows a low concentration of Q_5^5 units, an overcoordinated species quite unexpected but present in appreciable amount in the liquid. The distribution of Q_m^n units in our glass model is compared in Table II with those of models of alkali tellurite glasses at low alkali concentrations (10%–15%) obtained from a reverse Monte Carlo fit of neutron and x-ray diffraction data.[13] Unfortunately, an analogous reverse Monte Carlo analysis is not available for pure g-TeO_2. In the reverse Monte Carlo model of Ref. 13, the fitting of the total scattering function has been based on the structural units found in tellurite-based crystals, namely, the Q_3^0, Q_3^1, Q_3^2, Q_4^3, and Q_4^4 polyhedra. However, the glass model obtained from the fit also contains Q_3^3 units and a very tiny fraction of other polyhedra. Alkali-doped glasses show more cleaved bonds than our pure glass model, with less fully connected Q_m^m units and more terminal units Q_m^{m-r}. This is the expected effect on the glass network introduced by alkali doping.

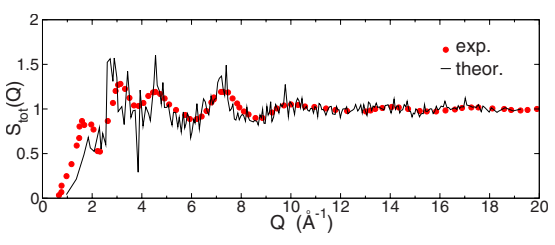

FIG. 15. (Color online) Theoretical total structure factor of TeO_2 glass compared with experimental neutron-scattering data (circles) from Ref. 6.

TABLE II. Distribution (%) of Q_m^n structural units in the g-TeO_2 at 300 K, averaged in time and on models A and B. Experimental data refer to alkali tellurite glasses of compositions $(Li_2O)_{0.15}(TeO_2)_{0.85}$, $(Na_2O)_{0.12}(TeO_2)_{0.88}$, and $(K_2O)_{0.10}(TeO_2)_{0.90}$ (Ref. 13).

	Q_3^0	Q_3^1	Q_3^2	Q_3^3	Q_4^3	Q_4^4	Q_5^5
Theor. (300 K)	0	0.6	14.9	20.4	17.1	35.9	9.4
Expt.	1–2	5–10	26–33	5–9	24–29	23–35	0

One would expect naively that two NBO are introduced by each Na_2O (in Na-doped glass). Actually the concentration of NBO inferred from the RMC model for alkali-doped glasses is larger than that expected from the simple argument given above. This is, however, consistent with the presence of a large number of NBO in pure g-TeO_2 as emerged from our simulation (cf. Table II). An equilibrium between intrinsic NBO and those produced by doping would then be achieved in alkali-doped glasses. By inspection in Table II one might conclude that the increase in NBO content in alkali-doped glasses might occur via the transformation of Q_3^3 into Q_3^2 units. This might account for the fact that, although we find a large fraction of Q_3^3 in our pure g-TeO_2 models, these units have never been considered in the interpretation of experimental data of alkali-stabilized glasses.

However, we have to consider also that the concentration of NBO in our model of g-TeO_2 might be larger than in reality due, perhaps, to a too high cooling rate used in the quenching protocol which might have prevented the system to reach a fully equilibrated glass structure. In other words, our g-TeO_2 model might show some remnants of the liquid structure from which it has been produced in terms of a concentration of NBO too close to that of the liquid. Actually, the analysis of the vibrational properties of our g-TeO_2 model given in Sec. V C seems to support this view. Similarly, a too high cooling rate from the melt, imposed by the computational constraints of *ab initio* simulations, is responsible for a too large concentrations of small rings (three and four membered) in *ab initio* models of amorphous silica.[41]

In Fig. 16 we report the angle distribution function resolved for different Q_m^n polyhedra. Only Q_4^n polyhedra display axial bonds with O–Te–O angles at ~165°. The equa-

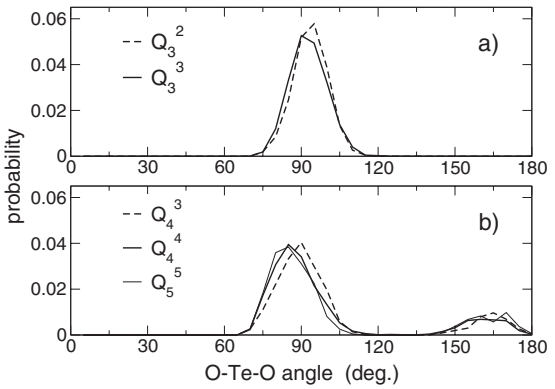

FIG. 16. Bond angle distribution of g-TeO_2 resolved for different polyhedra: (a) Q_3^n and (b) Q_4^n and Q_5^5 polyhedra.

torial bonds in Q_4^n units have a distribution centered slightly below 90°. The Q_3^n polyhedra show instead a single peak distribution centered slightly above 90°.

To assess the robustness of our definition of Q_m^n units, we have checked how the population of polyhedra in our glass model depends on the variation of the cutoff distance R_{max} used to define Te–O bonds. The result is shown in Fig. 17: the population of Q_m^n units in a configuration taken at random from the room-temperature simulation is poorly affected by variations of the R_{max} parameter in the range 2.34–2.38 Å. Still, at 300 K the librational motion of TeO_2 molecular units (O_{eq}–Te–O_{eq}) induces fluctuations in the Te–O_{ax} bond lengths sufficiently large to cross the cutoff distance R_{max} (Fig. 18). As a consequence, the instantaneous distribution of Q_m^n units fluctuates in time in our small sample (Fig. 19). Fluctuations in Te–O bond lengths up to 0.18 Å can be accounted for by harmonic phonons, as we have verified by computing the mean-square bond fluctuations $\langle|\mathbf{u}_\kappa - \mathbf{u}_{\kappa'}|^2\rangle$, where the $\langle\cdots\rangle$ indicate a thermal average obtained from harmonic phonons [Eq. (4)]. Harmonic stretching and bending modes of Te–O_{eq} bonds account for bond fluctuations of

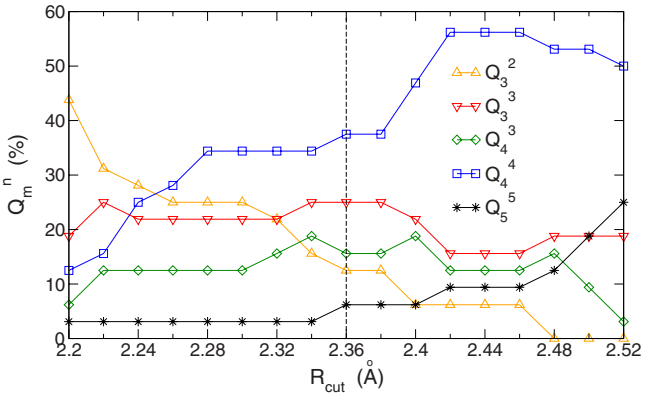

FIG. 17. (Color online) Variation of the Q_m^n population in g-TeO_2 as a function of the cutoff distance R_{max} used to define Te–O bonds for a snapshot geometry from the MD run at 300 K (populations can deviate from the average values in Table II). The vertical dashed line indicates the value R_{max}=2.36 Å adopted here and in Ref. 13. Only species in concentration larger than 1% are shown.

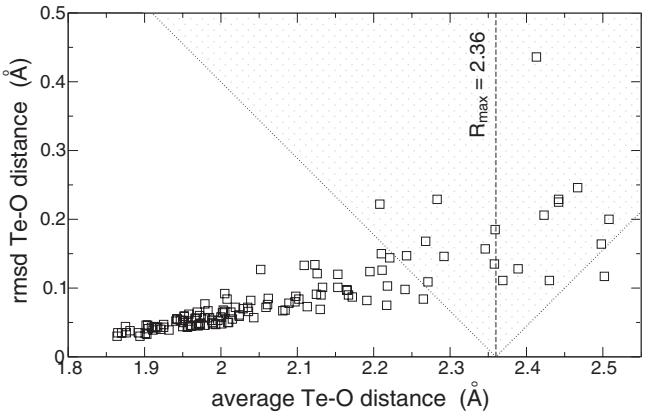

FIG. 18. Root-mean-square variation of Te–O distance as a function of the average Te–O distance for Te–O bonds in g-TeO_2 at 300 K. The vertical dashed line indicates the cutoff distance R_{max} =2.36 Å used in the definition of Q_m^n units (see text). The points in the shaded area correspond to Te–O bonds whose length fluctuates enough to cross back and forth the R_{max} threshold, leading to the fluctuations in the Q_m^n populations shown in Fig. 19.

shorter Te–O distances (<2.1 Å), while longer bonds are mostly affected by librational and translational harmonic modes. Fluctuations in Te–O bond lengths larger than 0.18 Å are due to anharmonic motions. We have also checked whether these latter anharmonicities might be due to the presence of metastable, not fully relaxed, local structures. To this aim we have further annealed the glass model at 1000 K for 13 ps and then quenched it down to room temperature in 8 ps. The latter model still shows fluctuations in time of the Q_m^n units similar to those reported in Figs. 18 and 19. We remark that for model B, quenched from the liquid on a much longer time, the fluctuations in time of Q_m^n units are very similar to those of Fig. 19. Therefore, we conclude that the large fluctuations in bond lengths at 300 K are not arti-

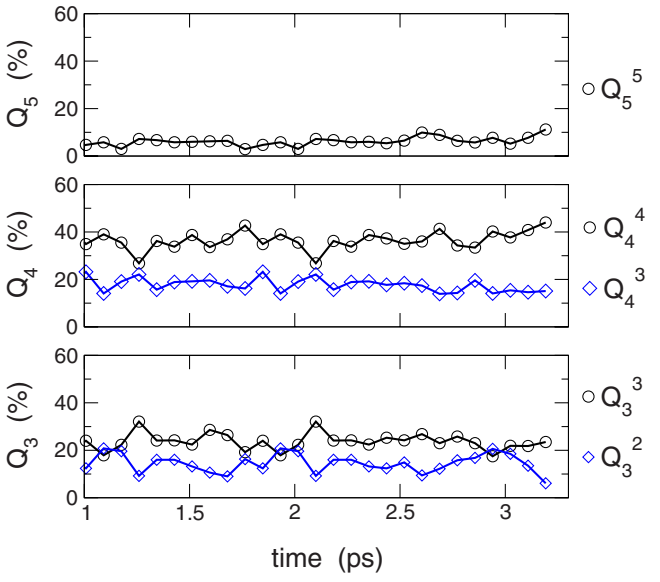

FIG. 19. (Color online) Evolution of the population of Q_m^n structural units as a function of time in g-TeO_2 at T=300 K. Only species in concentration larger than 1% are shown.

TABLE III. Number of rings $(TeO)_n$ of length n per 32 TeO_2 f.u. in the g-TeO_2 model and in the crystalline phases. Experimental values are the result of a reverse Monte Carlo fit of neutron-diffraction data of tellurite glass doped with 12 mol % Na_2O (Ref. 21).

	n										
	2	3	4	5	6	7	8	9	10	11	12
α-TeO_2	0	0	0	0	64	0	0	0	0	0	0
β-TeO_2	16	0	0	0	64	0	0	0	0	0	0
γ-TeO_2	0	0	0	0	64	0	0	0	0	0	0
TeO_2 glass (300 K)	2.7	4.1	1.5	2.4	1.6	3.9	3.6	3.9	5.5	6.7	5.1
Expt. (Na_2O 12%)	0.9	1.7	2.2	2.4	3.3						

facts of our quenching protocol, but they seem to be associated to the floppiness of some local structures in the glass which might be one of the sources of the poor stability of the pure glass toward recrystallization.

To further investigate the topology of the glass network, we have computed the distribution of rings formed by Te atoms bridged by O atoms, according to the shortest-path definition of Ref. 42. The ring distributions of our g-TeO_2 model and of the crystalline α, β, and γ phases are compared in Table III. Apparently, the glass model has a very low connectivity with respect to crystalline TeO_2. Snapshots of the structure of g-TeO_2 are given in Fig. 20. Evidence of a low connectivity of alkali-doped tellurite glass (12 mol % Na_2O) has been reported previously from a reverse Monte Carlo analysis of neutron-diffraction data.[21] The presence of Te–O–Te chains with a low 3D connectivity has also been proposed as the main source of the nonlinear dielectric properties of the glass on the basis of *ab initio* calculations of the dielectric response of small $(TeO_2)_n$ clusters.[43]

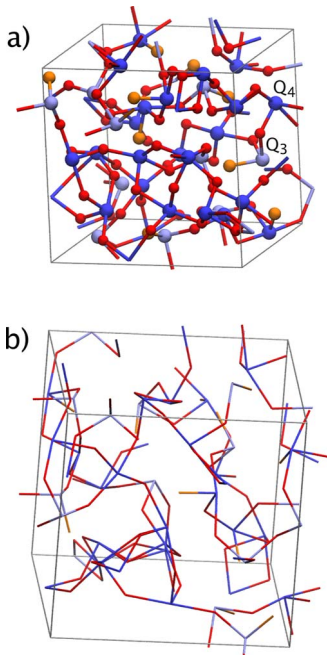

FIG. 20. (Color online) Structure of the 96-atom model of g-TeO_2. (a) Ball-stick and (b) stick views are reported. In panel (a), large dark (blue) and light (cyan) spheres represent Te in Q_4^n and Q_3^n polyhedra, respectively. Small dark (red) spheres are bridging O atoms. Small light (orange) spheres are nonbridging O atoms.

B. Electronic properties

The electronic density of states (DOS) of the g-TeO_2 model, as computed from Kohn-Sham energies at the Γ point of the supercell Brillouin zone, is reported in Fig. 21. The CPMD code and a plane-wave basis set for wave functions have been used (cf. Sec. III). The calculated highest occupied molecular orbital (HOMO)–lowest unoccupied molecular orbital (LUMO) gap is 2.51 eV, to be compared with the experimental optical (Tauc) band gap of 3.37 eV.[44] This sizable underestimation is not unexpected, being a common feature of DFT calculations. Similar results have been obtained for the (indirect) band gap of crystalline α-TeO_2 [E_g^{th}=2.8 eV, E_g^{expt}=3.5 eV (Ref. 45)].

Density of states projected on atomic pseudowave functions is shown in Fig. 21. The Kohn-Sham orbitals just below the valence-band maximum (HOMO-like) are mainly O p electrons not participating in Te–O bonds with some (small) admixture of the Te lone pairs. The empty LUMO-like states near the conduction-band edge are antibonding states of mixed O and Te characters, oriented in space in order to be orthogonal to the bonding orbitals in the valence band. This description of the orbitals near the band gap is in agreement with our findings on the tellurite crystalline phases[7] and with other first-principles calculations on the α phase.[20]

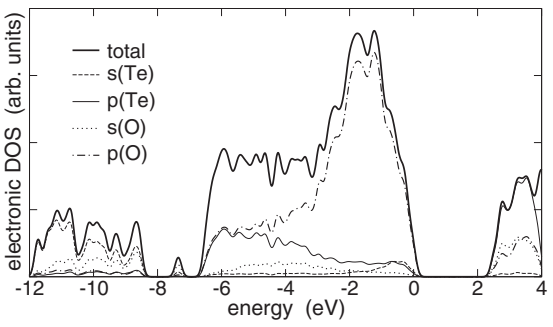

FIG. 21. Electronic density of states of the g-TeO_2 model from Kohn-Sham orbitals at the supercell Γ point. The zero of energy corresponds to top of the valence band. The projection of the DOS on s and p atomic wave functions of O and Te atoms is also shown. The Kohn-Sham energies have a Gaussian broadening of 0.1 eV.

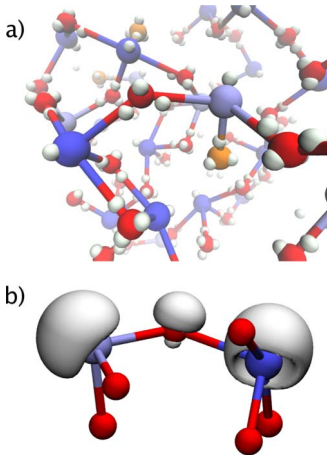

FIG. 22. (Color online) (a) Wannier centers (gray spheres) in the g-TeO_2 model. Large (blue) and small (red) dark spheres represent O and Te atoms, respectively. Near the front Q_3^2 and Q_4^4 units are clearly visible. (b) Selected Wannier isosurfaces enclosing 50% of the electronic charge.

To gain insight onto the chemical bonding of tellurite glass we have also computed maximally localized Wannier orbitals which are the periodic version of the Boys orbitals.[46] The Wannier orbitals are obtained by the unitary transformation of the Kohn-Sham occupied orbitals which minimizes the quadratic spread.[47,48]

Isosurfaces of the Wannier orbitals in our g-TeO_2 model are shown in Fig. 22. Four valence electron doublets are bonded to each O ion, more electronegative than Te. Actually, the Wannier orbitals have a large Gaussian spreading of $\sigma=0.876\pm0.028$ Å as defined by $\sigma=\sqrt{\langle\phi|r^2|\phi\rangle-|\langle\phi|\mathbf{r}|\phi\rangle|^2}$ (for sake of comparison $\sigma=0.768\pm0.031$ Å for O ions in the model of amorphous silica in Ref. 49). Each Te ion has in turn a doublet with a spread of $\sigma=1.155\pm0.020$ Å which corresponds to the lone pair at the opposite side of the Te–O bonds. The presence of a large and easily polarizable electronic doublet on Te ions, at variance for instance with silicon ions in silica glass, is usually considered as the main source of the large Raman cross section and strong nonlinear optical properties of tellurite glasses.

C. Vibrational properties

We have calculated the vibrational properties of pure tellurite glass in the framework of density-functional theory. Starting from the relaxed geometry of the as-quenched glass (model A), phonon frequencies have been obtained by diagonalizing the dynamical matrix obtained in turn from the variation of atomic forces due to finite atomic displacements of 0.02 Å large. Only phonons with the periodicity of our supercell (Γ point phonons) have been considered. However, since we are modeling the glassy phase with a periodic supercell, we can still define a $\mathbf{q}$-vector for the phononic modes for the glass model. The modes which display a dipole moment couple to the inner macroscopic longitudinal electric field which shifts phonon frequencies via the nonanalytic contribution to the dynamical matrix,[34]

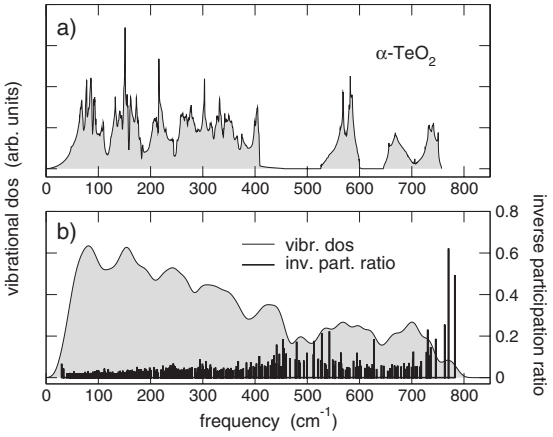

FIG. 23. (a) Theoretical vibrational density of states of α-TeO_2 (Ref. 7). (b) Vibrational density of states (shaded black line) of the g-TeO_2 model from phonons at the supercell Γ point. Phonon frequencies have a Gaussian broadening of 10 cm^{-1}. Superimposed it is shown the inverse participation ratio [spikes, Eq. (8)] of vibrational modes. The effect of the macroscopic electric field (LO–TO splitting) is not included.

$$D_{\alpha\beta}^{\mathrm{NA}}(\kappa,\kappa')=\frac{4\pi}{V_o}\frac{\sum_{\alpha'}Z_{\alpha\alpha'}(\kappa)q_{\alpha'}\sum_{\beta'}Z_{\beta\beta'}(\kappa')q_{\beta'}}{\mathbf{q}\cdot\underline{\underline{\epsilon}}^{\infty}\cdot\mathbf{q}}, \quad (6)$$

where $\underline{\underline{Z}}$ and $\underline{\underline{\epsilon}}^{\infty}$ are the effective charges and electronic dielectric tensor, V_o is the unit-cell volume, and $\mathbf{q}$ is the phononic wave vector. The macroscopic field contribution to the dynamical matrix [Eq. (6)] introduces a splitting between longitudinal and transverse optical modes (LO–TO splitting).

The high-frequency electronic dielectric tensor $\underline{\underline{\epsilon}}^{\infty}$ in Eq. (6) has been calculated within linear-response theory[34] and reads

$$\varepsilon=\begin{pmatrix}4.92 & 0.12 & 0.00\\ 0.12 & 4.80 & -0.01\\ 0.00 & -0.01 & 4.59\end{pmatrix}. \quad (7)$$

Due to the small size of our simulation cell, the tensor is not fully isotropic as it would be for a homogeneous glass. The calculated average value $\mathrm{tr}(\epsilon^{\infty})/3=4.77$ is slightly larger than the experimental value $\epsilon_{\mathrm{expt}}^{\infty}=4.4$, as usual within DFT. The experimental value is obtained from the measured refractive index $n_{\mathrm{expt}}=2.1$ above $\lambda\approx2$ μm.[44] Effective charges have been computed as well and the results are discussed at length in Sec. V D.

The vibrational DOS of the g-TeO_2 model is compared with the DOS of crystalline α-TeO_2 in Fig. 23. The inclusion of the macroscopic electric field (LO-TO splitting), calculated by diagonalizing the dynamical matrix with the nonanalytic part included [Eq. (6)], affects only marginally the vibrational DOS—as shown in Fig. 24—for selected directions of the phonon $\mathbf{q}$-vector which should be all equivalent for a homogeneous system. At variance with the DOS of α-TeO_2,[7] in the glass there is no gap between the low-frequency bending modes and the high-frequency stretching

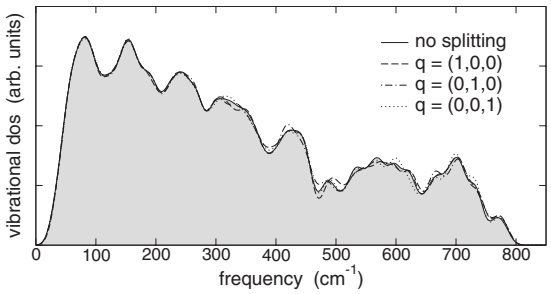

FIG. 24. Vibrational DOS of the g-TeO_2 model from phonons at the supercell Γ point, including LO-TO splittings for $\mathbf{q}$ along (0,0,1), (0,1,0), and (1,0,0). The vibrational spectrum without the contribution of the macroscopic electric field is drawn as the shaded curve for comparison. Phonon frequencies have a Gaussian broadening of 10 cm^{-1}.

modes, although a depletion in the DOS of g-TeO_2 can still be observed around 460 cm^{-1}.

In an amorphous material, phonons display localization properties which depend on frequency. To address this issue, we have computed the inverse participation ratio (IPR) of the jth vibrational mode (Fig. 23) defined as

$$\mathrm{IPR} = \frac{\sum_\kappa \left| \frac{\mathbf{e}(j,\kappa)}{\sqrt{M_\kappa}} \right|^4}{\left(\sum_\kappa \frac{|\mathbf{e}(j,\kappa)|^2}{M_\kappa} \right)^2}, \tag{8}$$

where $\mathbf{e}(j,\kappa)$ are phonon eigenvectors and the sum over κ runs over the N atoms in the unit cell. According to this definition the value of IPR varies from $1/N$ for a completely delocalized phonon to 1 for a mode completely localized on a single atom. The calculated IPR (Fig. 23) shows that most of the vibrational modes are delocalized on a large number of atoms, while few of them, above 400 cm^{-1}, are strongly localized and the highest in frequency are almost one-atom oscillations. To get further insight into the relationship between the vibrational spectrum and the structural units of the glass, the DOS has been projected on BO (86%) and NBO (14%) atoms (Fig. 25). It can be noted that due to the lighter

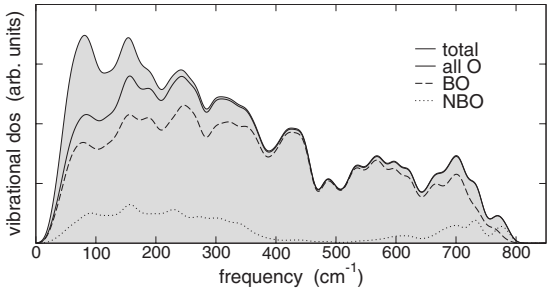

FIG. 25. The projections of the vibrational DOS of g-TeO_2 on all O atoms (black line), bridging O atoms (BO, dashed line), and nonbridging O atoms (NBO, dotted line) are reported together with the total DOS (shaded dashed curve). The effect of the macroscopic electric-field (LO-TO splitting) is not included. Phonon frequencies have a Gaussian broadening of 10 cm^{-1}.

mass, the O atoms contribute much more than Te atoms to the displacement patterns especially for $\omega > 200$ cm^{-1}. The projection on BO contributes for nearly 100% of the DOS between 400 and 650 cm^{-1}. On the other hand, above 750 cm^{-1} the spectrum is dominated by vibrations well localized on NBO (cf. Figs. 23 and 25). This is consistent with the fact that NBO are expected to be more strongly bonded to Te ions than BO. Indeed the Te–O bond length of NBO is sizably shorter (1.874 ± 0.020 Å) than the average length of the equatorial Te–O_{eq} bonds (1.95 Å).

The relative contribution of each Q_m^n unit to the stretching part of the vibrational spectrum of the glass is shown in Fig. 27, as computed by projecting phonon displacement patterns along Te–O bonds belonging to different Q_m^n units. At frequencies below 750 cm^{-1} the relative contribution of the five Q_m^n units simply reflects their abundance in the glass (see Table II). At higher frequencies, Q_4^3 and Q_3^2 units play a major role since they are the only structures containing NBO, which dominate the spectrum above 750 cm^{-1} (see Fig. 25). In the experimental literature[37,50] it is often proposed a tentative partition of the stretching part of the vibrational spectrum in a low-frequency region due to stretching of the Q_4 units and a higher frequency region due to Q_3 stretching. Overall, our analysis indicates that it is not possible to assign vibrations of different Q_m^n units to different spectral ranges. A clear separation in frequency exists for BO and NBO stretchings but not among BO stretching of Q_4 and Q_3 units. In Fig. 27 we also report the DOS projected on stretching modes of short (<2 Å) and long (>2 Å) Te–O bonds, which correspond, respectively, to equatorial and axial bonds in crystalline TeO_2. Around 550 cm^{-1}, we recognize a threshold frequency above which the main contribution to the DOS changes character from stretching modes of equatorial (shorter) bonds to stretching of axial (longer) bonds.

A different insightful decomposition of the DOS is obtained by considering the displacements of BO along three different directions in space: the direction linking the two Te atoms of the Te–O–Te bridge, the perpendicular direction in the Te–O–Te plane, and the direction perpendicular to the latter plane [inset of Fig. 27(a)]. These three displacements can be associated to stretchings of Te–O bonds and bending and librations of Te–O–Te bridges, respectively. Projection of the DOS along these BO displacements reveals that (i) the DOS above 500 cm^{-1} is mostly due to Te–O stretchings, (ii) bendings of the Te–O–Te bridge sizably contribute to the peak at ~420 cm^{-1}, and (iii) librations of the Te–O–Te bridges dominate the DOS in the range 200–300 cm^{-1}. Complementary information for the assignment of the DOS to specific phonons is gained by projecting the DOS onto the molecular modes of the TeO_2 units $O_{eq}TeO_{eq}$ in the Q_4^4 polyhedra, easily identified since the $O_{ax}TeO_{ax}$ angles are much larger than the $O_{eq}TeO_{eq}$ and $O_{eq}TeO_{ax}$ ones as already pointed out in Sec. IV A. There are 21 Q_4^4 polyhedra and then 21 TeO_2 molecular units in our g-TeO_2 model. Projection of the vibrational DOS on translational, librational, bending, and stretching modes of the TeO_2 molecular units is reported in Fig. 26. Molecular bendings mostly contribute to the peak at ~400 cm^{-1}. Translations, librations, and stretchings contribute to the spectral ranges 0–200, 200–400, and 500–800 cm^{-1}, respectively.

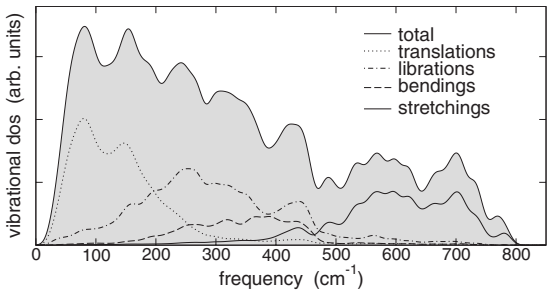

FIG. 26. Projection of the vibrational density of states on the normal modes of the $Te(O_{eq})_2$ molecules (see text): translations, librations, bendings, and stretchings. Phonon frequencies have a Gaussian broadening of 10 cm^{-1}.

D. Infrared spectra

The average isotropic Born effective charge is defined as $\langle Z\rangle = \mathrm{tr}(Z)/3$. In our g-TeO_2 model the values of $\langle Z\rangle$ are (average $\pm$ rms deviation in a.u.) 4.725 ± 0.409 for Te, -2.391 ± 0.186 for BO, and -2.183 ± 0.223 for NBO. Both the average values and the spreads are very large. [For sake of comparison the effective charges in silica glass are 3.177 ± 0.121 for Si and -1.588 ± 0.078 for O (Ref. 51)]. This feature is due to the presence of large and easily polarizable nonbonding electron pairs both on O and Te atoms, together with the variety of coordination polyhedra around Te atoms, which leads to a wealth of different local environments. On the other hand we have been unable to associate the large variations in the values of $\langle Z\rangle$ with simple local descriptors such as bond lengths, Te–O–Te or O–Te–O angles, Q_m^n units, etc. Actually even for BO/NBO the distributions of $\langle Z\rangle$ are heavily overlapping. The large spread of the effective charges of both NBO and BO recalls a similarly large spread in XPS and ^{17}O NMR signals which prevented the discrimination between BO and NBO.[52]

It is possible to characterize the anisotropy of the effective charge tensor Z by comparing the invariant $\mathrm{tr}(Z)$ with a bracket $\hat{\mathbf{n}}^T Z \hat{\mathbf{n}}$, where $\hat{\mathbf{n}}$ is a Cartesian versor chosen along a direction of local atomic symmetry. In the isotropic case any direction $\hat{\mathbf{n}}$ would equally contribute $\mathrm{tr}(Z)/3$. For Te atoms we choose the direction which defines the plane perpendicular to O–Te–O units. This plane passing through the Te atom divides the space into two, half containing the Te–O bonds and the other half containing the lone electron pair. This direction contributes 27% to $\mathrm{tr}(Z)$; thus the orthogonal directions in the O–Te–O plane give the largest contribution. For each BO three orthogonal versors can be identified, as described in Sec. V C and Fig. 27(a): the first is along the Te–Te direction, the second lies in the Te–O–Te plane and is orthogonal to the first, and the third is normal to the Te–O–Te plane. These three directions contribute, respectively, 56%, 26%, and 18% to $\mathrm{tr}(Z)$; thus the motion of the BO along the Te–Te direction produces the largest modulation of the dipole moment (as expected since Te–O–Te angles are typically larger than 90°). Finally the direction along the Te–O bond contributes for 47% to $\mathrm{tr}(Z)$ of NBO.

In Fig. 28 we report the calculated complex dielectric function,

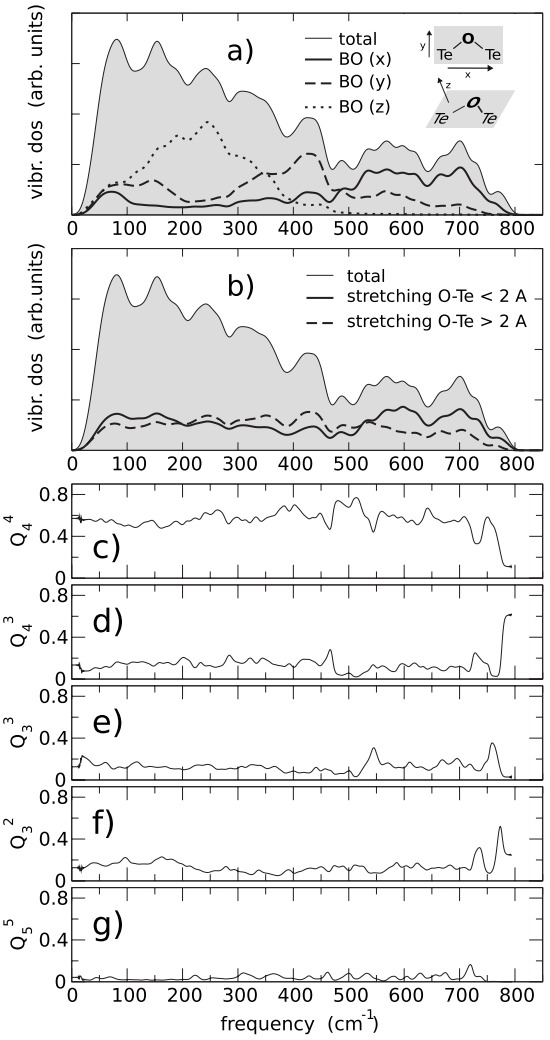

FIG. 27. (a) The vibrational DOS of g-TeO_2 projected on BO. For each O atom the eigenmodes are projected along the three directions sketched in the inset: along Te–Te (x) of the Te–O–Te bridge, normal to the latter in the Te–O–Te plane (y), and normal to the Te–O–Te plane (z). (b) Projection on stretchings of short (equatorial-like, <2 Å) and long (axial-like, >2 Å) Te–O bonds. (c)–(g). The relative contribution to the projection on Te–O stretchings from the five types of Q_m^n units present in the glass model. Phonon frequencies have a Gaussian broadening of 10 cm^{-1}.

$$\epsilon(\omega) = \epsilon^{\infty} + \frac{4\pi}{3V_0}\sum_j \frac{|\mathbf{F}^j|^2}{\omega_j^2 - (\omega + i\gamma)^2}, \tag{9}$$

$$F_\alpha^j = \sum_{\kappa=1}^{N}\sum_{\beta} Z_{\alpha\beta}(\kappa)\frac{e_\beta(j,\kappa)}{\sqrt{M_\kappa}}, \tag{10}$$

where the vibrational eigenfrequencies ω_j and eigenvectors $e_\beta(j,\kappa)$ do not include the effect of the macroscopic electric field. V_o is the unit-cell volume and γ is set to 20 cm^{-1}.

The IR absorption coefficient is given by

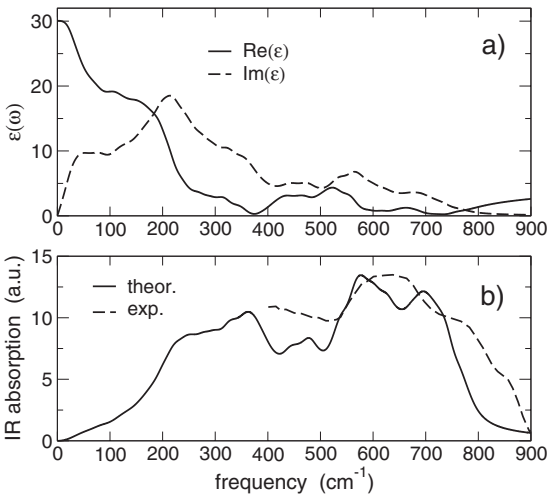

FIG. 28. (a) Dielectric function $\epsilon(\omega)$ (real and imaginary parts). (b) Theoretical IR absorption spectrum $\alpha(\omega)$ in atomic units compared with the experimental data (Ref. 18). The experimental intensities are rescaled to the maximum of the theoretical spectrum.

$$\alpha(\omega) = \frac{\omega}{c}\frac{\epsilon_2(\omega)}{n_1(\omega)}, \tag{11}$$

where $\epsilon_2 = \mathrm{Im}(\epsilon)$ and $n_1 = \mathrm{Re}(\sqrt{\epsilon})$. In Fig. 28 we compare the theoretical and experimental[18] IR spectra of TeO_2 glass. The experimental IR intensity is tentatively set to zero at 900 cm^{-1} in the lack of absolute experimental IR intensities. This choice might have enhanced the experimental IR peaks over a background intensity. A redshift of the theoretical spectrum with respect to experiments is to be expected due to inaccuracies in the description of bonding in tellurite systems by DFT generalized gradient approximation (GGA) as discussed in Ref. 7 for crystalline TeO_2.

The calculated value of ϵ_0 is anomalously large ($\sim$30) and much larger than the experimental result ($\sim$20 at room temperature[1]). This discrepancy is not to be attributed to deficiencies in our DFT-GGA framework since for crystalline α-TeO_2 our previous phonon calculation yielded $\epsilon_0 = 22.9$,[7] a value very close to the experimental result of 24.9.[53] Actually by resolving the dielectric function in the contribution from different phonons, we have found that the upraise of $\epsilon(\omega)$ below 100 cm^{-1} is due to phonons responsible for the fluctuations in the distribution of Q_n^m polyhedra reported in Sec. V A. These modes are strongly anharmonic as discussed in Sec. V A and their zero-temperature harmonic frequencies are probably underestimated with respect to the finite temperature values. A self-consistent phonon calculation at finite temperature, which is however outside the scope of the present work, might bring the theoretical static dielectric constant to a better agreement with experiments.

E. Raman spectra

The differential cross section for Raman scattering (Stokes) in nonresonant conditions is given by the following expression (for a unit volume of scattering sample):

$$\frac{d^2\sigma}{d\Omega d\omega} = \sum_j \frac{\omega_S^4}{c^4}|\mathbf{e}_S \cdot \underline{\underline{R}}^j \cdot \mathbf{e}_L|^2[n_B(\omega)+1]\delta(\omega-\omega_j), \tag{12}$$

where $n_B(\omega)$ is the Bose factor, ω_S is the frequency of the scattered light, and $\mathbf{e}_S$ and $\mathbf{e}_L$ are the polarization vectors of the scattered and incident light, respectively.[54,55] The Raman tensor $\underline{\underline{R}}^j$ associated with the jth phonon is given by

$$R^j_{\alpha\beta} = \sqrt{\frac{V_o\hbar}{2\omega_j}}\sum_{\kappa=1}^{N}\frac{\partial\chi^\infty_{\alpha\beta}}{\partial\mathbf{r}(\kappa)}\cdot\frac{\mathbf{e}(j,\kappa)}{\sqrt{M_\kappa}}, \tag{13}$$

where $\mathbf{r}(\kappa)$ is the position of the κth atom and $\underline{\underline{\chi}}^\infty = (\underline{\underline{\epsilon}}^\infty - \underline{\underline{1}})/4\pi$ is the electronic susceptibility.

We have considered only phonons with frequency higher than 200 cm^{-1}. The Raman response of g-TeO_2 has been obtained from finite variations of $\chi^\infty_{\alpha\beta}$ along phonon eigenmodes with maximum atomic displacement of 0.02 Å. The scattering wave vector $\mathbf{q}$ and the incoming and outgoing polarization vectors $\mathbf{e}_L$ and $\mathbf{e}_S$ [Eq. (12)] have been averaged numerically over 4096 different orientations to compare with the experimental isotropic unpolarized Raman spectrum in backscattering setup; the effect of the macroscopic electric-field (LO-TO splitting) on the phonon eigenvalues and eigenvectors has to be included by diagonalizing the complete dynamical matrix containing the nonanalytic term [Eq. (6)] for each scattering wave vector $\mathbf{q}$. We computed once and for all the Raman tensors $\underline{\underline{R}}^m_o$ relative to the mth phonon without the nonanalytic term $[\mathbf{e}^o(m,\kappa)]$, then we obtained the corresponding Raman tensors $\underline{\underline{R}}^j(\mathbf{q}\to 0)$ including the nonanalytic term by a rotation,

$$\underline{\underline{R}}^j = \sqrt{\frac{V_0\hbar}{2\omega_j}}\sum_{\alpha\kappa}\frac{\partial\underline{\underline{\chi}}^\infty}{\partial r_{\alpha\kappa}}\frac{e_\alpha(j,\kappa)}{\sqrt{M_\kappa}} = \sum_m\left(\sqrt{\frac{\omega^o_m}{\omega_j}}\sum_{\beta\kappa}e^o_\beta(m,\kappa)\cdot e_\beta(j,\kappa)\right)\underline{\underline{R}}^m_o, \tag{14}$$

where j (m) is the phonon index and the κ runs over the N atoms in the simulation cell.

In principle this transformation requires the unperturbed Raman tensors $\underline{\underline{R}}^n_o$ to be available for all phonons to get the exact coefficients $\partial\underline{\underline{\chi}}^\infty/\partial\mathbf{r}_\alpha$ for all atoms. In practice, the restriction [in the sum over m in Eq. (14)] to modes with frequency over 200 cm^{-1} does not introduce sizable errors because the subspace spanned by the vectors $\mathbf{e}^o(m)$ with $\omega^o_m > 200$ cm^{-1} overlaps for more than 99% with the subspace spanned by the $\mathbf{e}(n)$ modified by the macroscopic field [Eq. (6)] for all wave vectors $\mathbf{q}$. This procedure allows obtaining the Raman spectrum restricted to the most interesting spectral region with a number of derivatives of the electronic polarizability sizably smaller than $3N$.

The calculated Raman spectrum is reported in Fig. 29. The effect of the macroscopic electric field is overall small on the Raman spectrum as shown in Fig. 29(d). The linewidths of the Raman peaks affect the overall shape of the spectrum. We have not attempted to compute the linewidths theoretically. Instead, we have assigned a Lorentzian linewidth as a function of frequency by interpolating the available experimental linewidths of the Raman peaks in poly-

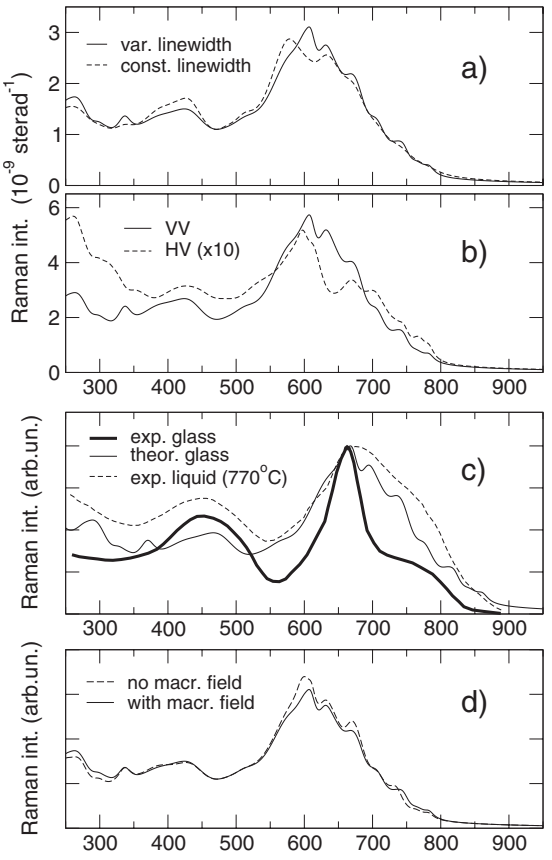

FIG. 29. (a) Theoretical Raman spectrum of tellurite glass in the unpolarized backscattering setup with a frequency independent linewidth of 20 cm^{-1} (dotted line) or a variable linewidth (continuous line) fitted to experimental Raman spectra of crystalline TeO_2 (see text and Fig. 30). (b) Theoretical Raman spectra of g-TeO_2 for incoming and outgoing photons with parallel (VV) and perpendicular (HV) polarizations. A frequency-dependent linewidth is used as in panel (a). The absolute Raman differential scattering cross section (without the Bose occupation factor) is reported for the theoretical spectra. (c) Experimental Raman spectra of tellurite glass (solid line) and of liquid TeO_2 (dashed line) (Ref. 18) at 770 °C are compared with the theoretical Raman spectrum with frequencies scaled by a factor 1.1 (see text) and the frequency-dependent linewidth as in panels (a) and (b). All the theoretical and experimental spectra are obtained for a laser frequency of 514.5 nm (Ar laser). For g-TeO_2 $T=300$ K. (d) Theoretical Raman spectra with and without the contribution of the macroscopic electric field (see text).

crystalline α, β, and γ-TeO_2 (Ref. 10) (see Fig. 30). To compare the theoretical and experimental spectra of TeO_2 glass, we have to consider also the inhomogeneous broadening induced by disorder, which we can only partially account for by a calculation with a small cell at the Γ point. To account for the latter effect, we have doubled the homogeneous linewidths obtained from the data on the crystalline phases (Fig. 30). For the sake of comparison we also report the Raman spectrum with a frequency-independent linewidth of 20 cm^{-1} chosen such as to reproduce the best overall agreement with the experimental Raman spectrum.

In both cases (constant or frequency-dependent linewidth) the overall shape of the calculated Raman spectrum is in fairly good agreement with experiments. In particular, the

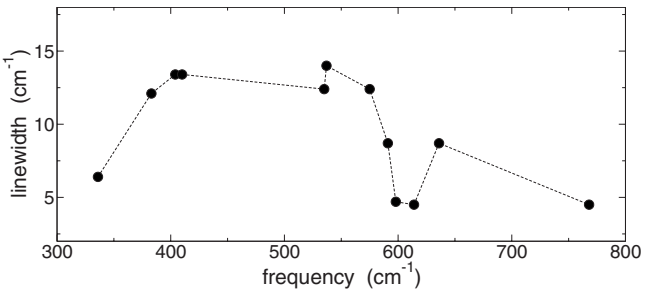

FIG. 30. Linewidth of the most intense experimental Raman peaks of α-, β-, and γ-TeO_2 polycrystals (Ref. 10). The frequencies correspond to the theoretical data of Ref. 7. The interpolated dashed line has been used to assign the linewidths of the Raman peaks in g-TeO_2 (cf. Fig. 29).

relative intensity of the two main Raman peaks around 420 cm^{-1} (experimental: 450 cm^{-1}) and 590 cm^{-1} (experimental: 660 cm^{-1}) is well reproduced.

The main discrepancy is an $\approx$10% redshift of the bands which can be traced back to inaccuracies in the description of bonding in tellurite systems by DFT-GGA as discussed in Ref. 7 for crystalline TeO_2. A good agreement between experimental and theoretical Raman spectra is obtained by rescaling the *ab initio* frequencies by a factor 1.1 [Fig. 29(c)]. From the projected vibrational spectrum in Fig. 27 the Raman peak at 420 cm^{-1} can be assigned mainly to Te–O–Te bendings. Similarly, from Fig. 27 the peak around 600 cm^{-1} is mainly due to stretchings of the Te–O–Te bridges (this applies also to the shoulder centered near 700 cm^{-1}). However, the wide experimental shoulder in the range 720–820 cm^{-1} (redshifted by 50 cm^{-1} in the theoretical spectrum) still appears much more pronounced in the *ab initio* spectrum. Actually, the shoulder is remarkably similar in relative intensity to the analogous structure present in the experimental spectrum of liquid TeO_2 [Fig. 29(c)] and Li_2O–TeO_2 glasses.[50] In alkali-doped glasses the intensity of the high-frequency shoulder increases with the alkali content, turning the Raman spectrum more and more similar to the spectrum of our pure g-TeO_2 model. Since both melting and alkali doping are expected to cleave a fraction of Te–O bonds, one would ascribe a higher intensity of the shoulder to an increase in the number of NBO in "defective" units Q_4^3 and Q_3^2 in liquid TeO_2 and alkali-doped glasses. However, the projected vibrational DOS (Fig. 25) shows that the high-frequency shoulder is mainly due to bridging O atoms while it has only a minor contribution from terminal O atoms (NBO). Thus, the shoulder cannot be easily assigned to vibrations of Q_4^3 or Q_3^2 units, which prevail only in the highest frequency tail of the DOS. Nevertheless, since phonons in this spectral region are largely delocalized, it is possible that a larger concentration of Q_4^3 and Q_3^2 units might still enhance the intensity of the high-frequency shoulder. Would it be the case, one should conclude that the concentration of these units is too large in our glass model, perhaps as a consequence of the extremely high cooling rate which has somehow frozen the larger abundance of these units typical of the liquid phase. This hypothesis would explain the similarity between the theoretical Raman spectrum of the glass and the

experimental spectra of liquid and alkali-doped glasses. However, the lack of reliable homogeneous (anharmonic) linewidths for the vibrational peaks of g-TeO_2 can also possibly contribute to the discrepancies between the theoretical and experimental Raman spectra.

The calculated peak Raman intensity of our g-TeO_2 model is 5.74×10^{-9} sr^{-1} (backscattering VV setup, 514.5 nm laser, without Bose occupation factor), i.e., 26 times the peak intensity of a-SiO_2.[56,57] Glasses stabilized with transition metals (e.g., Nb and W) display an enhancement of the Raman cross section with respect to a-SiO_2 (ratio of the strongest peak intensities) ranging from 25 to 180 depending on composition and laser wavelength.[2,58,59] The dependence on laser wavelength has been ascribed to the occurrence of resonances with electronic excitations induced by the presence of the stabilizer.[60] By increasing the wavelength of the laser up to 1064 nm, the Raman intensity converges to resonance-free values of 25 and 30 times larger than that of a-SiO_2, respectively, for $(TeO_2)_{0.85}(WO_3)_{0.15}$ and $(TeO_2)_{0.85}(Nb_2O_5)_{0.10}(MgO)_{0.05}$ (backscattering VV setup).[60] Our calculations indicate that g-TeO_2 has a Raman-scattering intensity similar to stabilized tellurite glasses in nonresonant conditions.

As a further comparison with experiments, we have computed the absolute Raman cross section of the most intense peak of crystalline α-TeO_2 (A1 mode at 649 cm^{-1}).[7] The theoretical Raman cross section of 1.97×10^{-7} sr^{-1} is 34 times larger than the peak in our g-TeO_2 model and 36 times larger than the 467 cm^{-1} mode of α quartz[56,57] (all these data refer to a 514.5 nm laser). This result is in agreement with experiments reporting that the Raman intensity of α-TeO_2 is as large as 40 times the maximum intensity of α quartz,[53] although lack of details on how such ratio has been measured prevents a fully compelling comparison between theory and experiments.

VI. CONCLUSIONS

We have generated a model of TeO_2 glass by fast quenching from the melt within *ab initio* molecular-dynamics simulations. Although no experimental data to compare with are available for pure liquid TeO_2, for future reference we have first fully analyzed the structural properties of the liquid phase at 2400 and 1000 K. The Q_4^4 polyhedra are the most abundant at both temperatures with percentages of 17% and 30% at 2400 and 1000 K, respectively. The polyhedra are, however, short lived with average lifetimes of 50 and 150 fs at high and low temperatures. TeO_2 molecular units (defined by the equatorial bonds) have similar lifetime as the polyhedra.

The glass model displays a variety of Q_m^n units with the predominance of Q_4^4 polyhedra (36%) typical of the crystalline phases. The glassy network is somehow less connected than the crystalline phases as inferred from the presence of very large rings in the glass structure. The different Q_m^n units can hardly be discriminated on the basis of local observables such as effective charges, localized Wannier functions, or localized phonon modes. On the contrary the presence of nonbridging O atoms in Q_m^n units with $n<m$ gives rise to strongly localized vibrational modes at high frequency (>700 cm^{-1}). The calculated Raman and IR spectra are in good agreement with available experimental data but for a redshift of the of theoretical bands which can be traced back to inaccuracies in the description of bonding in tellurite systems by DFT-GGA as previously discussed for crystalline TeO_2.[7] The absolute Raman cross section has been estimated as well to provide a reference number for pure TeO_2 in the search for suitable doped tellurite glasses with larger Raman response.

ACKNOWLEDGMENTS

This work was partially supported by Cineca through the CNISM-CNR-INFM Parallel Computing Initiative. Discussions with G. Dai and F. Tassone are gratefully acknowledged. We thank F. Zipoli for assistance in the use of the CP2K suite of programs and M. Krack for providing us with pseudopotentials and basis sets.

*Present address: Sissa, Via Beirut 2-4, I-34014 Trieste, Italy.
†Present address: Department of Chemistry and Applied Biosciences, ETHZ, USI-Campus, CH-6900 Lugano, Switzerland.

[1] R. A. H. El-Mallawany, *Tellurite Glasses Handbook* (CRC, Boca Raton, 2002).
[2] D. Dai, F. Tassone, A. Li Bassi, V. Russo, C. E. Bottani, and D. D'Amore, IEEE Photonics Technol. Lett. **16**, 1011 (2004).
[3] C. Rivero, K. Richardson, R. Stegeman, G. Stegeman, T. Cardinal, E. Fargin, M. Couzi, and V. Rodriguez, J. Non-Cryst. Solids **345&346**, 396 (2004).
[4] S. Coste, A. Lecomte, P. Thomas, J. C. Champarnaud-Mesjard, T. Merle-Mejean, and R. Guinebretiere, J. Non-Cryst. Solids **345-346**, 634 (2004).
[5] S. N. B. Hodgson and L. Weng, J. Mater. Sci.: Mater. Electron. **17**, 723 (2006).
[6] H. Niida, T. Uchino, J. Jin, S. H. Kim, T. Fukunaga, and T. Yoko, J. Chem. Phys. **114**, 459 (2001).
[7] M. Ceriotti, F. Pietrucci, and M. Bernasconi, Phys. Rev. B **73**, 104304 (2006).
[8] L. D'Alessio, F. Pietrucci, and M. Bernasconi, J. Phys. Chem. Solids **68**, 438 (2007).
[9] S. Blanchandin, P. Marchet, P. Thomas, J. C. Champarnaud-Mesjard, and B. Frit, J. Mater. Chem. **9**, 1785 (1999).
[10] J. C. Champarnaud-Mesjard, S. Blanchandin, P. Thomas, A. P. Mirgorodsky, T. Merle-Mejean, and B. Frit, J. Phys. Chem. Solids **61**, 1499 (2000).
[11] S. Sakida, S. Hayakawa, and T. Yoko, J. Non-Cryst. Solids **243**, 1 (1999).
[12] S. Sakida, S. Hayakawa, and T. Yoko, J. Non-Cryst. Solids **243**, 13 (1999).
[13] J. C. McLaughlin, S. L. Tagg, and J. W. Zwanziger, J. Phys. Chem. B **105**, 67 (2001).

[14] P. A. Thomas, J. Phys. C **21**, 4611 (1988).
[15] V. H. Beyer, Z. Kristallogr. **124**, 228 (1967).
[16] O. Noguera, Ph.D. thesis, University of Limoges, 2003; http://www.unilim.fr/scd/
[17] J. C. Champarnaud-Mesjard, S. Blanchandin, P. Thomas, A. P. Mirgorodsky, T. Merle-Méjean, and B. Frit, J. Phys. Chem. Solids **61**, 1499 (2000).
[18] O. Noguera, T. Merle-Mejean, A. P. Mirgorodsky, M. Smirnov, P. Thomas, and J. C. Champarnaud-Mesjard, J. Non-Cryst. Solids **330**, 50 (2003).
[19] B. R. Sahu and L. Kleinman, Phys. Rev. B **69**, 193101 (2004).
[20] E. Menendez-Proupin, G. Gutierrez, E. Palmero, and J. L. Pena, Phys. Rev. B **70**, 035112 (2004).
[21] J. C. McLaughlin, S. L. Tagg, J. W. Zwanziger, D. R. Haeffner, and S. D. Shastri, J. Non-Cryst. Solids **274**, 1 (2000).
[22] J. Sarnthein, A. Pasquarello, and R. Car, Phys. Rev. Lett. **74**, 4682 (1995).
[23] J. Sarnthein, A. Pasquarello, and R. Car, Phys. Rev. B **52**, 12690 (1995).
[24] S. Blanchandin, P. Marchet, P. Thomas, J. C. Champarnaud-Mesjard, B. Frit, and A. Chagraoui, J. Mater. Sci. **34**, 4285 (1999).
[25] A. D. Becke, Phys. Rev. A **38**, 3098 (1988).
[26] C. Lee, W. Yang, and R. G. Parr, Phys. Rev. B **37**, 785 (1988).
[27] G. Lippert, J. Hutter, and M. Parrinello, Theor. Chem. Acc. **103**, 124 (1999).
[28] J. VandeVondele, M. Krack, F. Mohamed, M. Parrinello, T. Chassaing, and J. Hutter, Comput. Phys. Commun. **167**, 103 (2005).
[29] CP2K, freely available, released under GPL license, http://cp2k.berlios.de
[30] S. Goedecker, M. Teter, and J. Hutter, Phys. Rev. B **54**, 1703 (1996).
[31] T. D. Kühne, M. Krack, F. R. Mohamed, and M. Parrinello, Phys. Rev. Lett. **98**, 066401 (2007).
[32] N. Troullier and J. L. Martins, Phys. Rev. B **43**, 1993 (1991).
[33] CPMD, Copyright IBM Corp. 1990–2005, Copyright MPI für Festkörperforschung Stuttgart 1997–2001, http://www.cpmd.org.
[34] S. Baroni, S. De Gironcoli, A. Dal Corso, and P. Giannozzi, Rev. Mod. Phys. **73**, 515 (2001).
[35] R. Car and M. Parrinello, Phys. Rev. Lett. **55**, 2471 (1985).
[36] D. A. Keen, J. Appl. Crystallogr. **34**, 172 (2001).
[37] R. Akagi, K. Handa, N. Ohtori, A. C. Hannon, M. Tatsumisago, and N. Umesaki, J. Non-Cryst. Solids **256&257**, 111 (1999).
[38] J. Kieffer, J. A. Johnson, O. Nickolayev, and J. D. Bass, J. Phys.: Condens. Matter **18**, 903 (2006).
[39] NIST-National Institute of Standards and Technology, http://physics.nist.gov/PhysRefData/
[40] L. Giacomazzi, P. Umari, and A. Pasquarello, Phys. Rev. B **74**, 155208 (2006).
[41] A. Pasquarello and R. Car, Phys. Rev. Lett. **80**, 5145 (1998).
[42] D. S. Franzblau, Phys. Rev. B **44**, 4925 (1991).
[43] A. P. Mirgorodsky, M. Soulis, P. Thomas, T. Merle-Méjean, and M. Smirnov, Phys. Rev. B **73**, 134206 (2006).
[44] S. H. Kim, T. Yoko, and S. Sakka, J. Am. Ceram. Soc. **76**, 2486 (1993).
[45] A. Svane and E. Antoncik, J. Phys. Chem. Solids **48**, 171 (1987).
[46] S. F. Boys, Rev. Mod. Phys. **32**, 296 (1960).
[47] N. Marzari and D. Vanderbilt, Phys. Rev. B **56**, 12847 (1997).
[48] P. L. Silvestrelli, N. Marzari, D. Vanderbilt, and M. Parrinello, Solid State Commun. **107**, 7 (1998).
[49] D. Donadio, M. Bernasconi, and F. Tassone, Phys. Rev. B **70**, 214205 (2004).
[50] M. Tatsumisago, S.-K. Lee, T. Minami, and Y. Kowada, J. Non-Cryst. Solids **177**, 154 (1994).
[51] A. Pasquarello and R. Car, Phys. Rev. Lett. **79**, 1766 (1997).
[52] R. T. Hart, J. W. Zwanziger, U. Werner-Zwanziger, and J. R. Yates, J. Phys. Chem. A **109**, 7636 (2005).
[53] A. S. Pine and G. Dresselhaus, Phys. Rev. B **5**, 4087 (1972).
[54] *Light Scattering in Solid*, edited by M. Cardona and G. Güntherodt (Springer-Verlag, Berlin, 1982).
[55] P. Brüesch, *Phonons: Theory and Experiments II* (Springer-Verlag, Berlin, 1986).
[56] R. H. Stolen and E. P. Ippen, Appl. Phys. Lett. **22**, 276 (1973).
[57] V. S. Gorelik and M. M. Sushchinskii, Sov. Phys. Solid State **12**, 1157 (1970).
[58] R. Stegeman, L. Jankovic, H. Kim, C. Rivero, G. Stegeman, K. Richardson, P. Delfyett, Y. Guo, A. Schult, and T. Cardinal, Opt. Lett. **28**, 1126 (2003).
[59] V. G. Plotnichenko, V. O. Sokolov, V. V. Koltashev, E. M. Dianov, I. A. Grishin, and M. F. Churbanov, Opt. Lett. **30**, 1156 (2005).
[60] C. Rivero, R. Stegeman, M. Couzi, D. Talaga, T. Cardinal, K. Richardson, and G. Stegeman, Opt. Express **13**, 4759 (2005).